Sustainable Energy & Fuels

ROYAL SOCIETY OF CHEMISTRY

PAPER

View Article Online
View Journal | View Issue

Cite this: *Sustainable Energy Fuels*, 2025, **9**, 6751

Towards a wide bandgap absorber: structural, morphological, and optical investigation of Ag-alloyed Cu_2ZnSnS_4 thin films

Messaoud Tamin, [ab] Outman El Khouja, [c] Mohamed Guemmaz, [a] Charif Tamin, [d] Amelia Elena Bocirnea, [e] Ilhame Asshsahi, [f] Denis Chaumont [b] and Aurelian Catalin Galca *[cg]

Wide band gap semiconductors are essential for next-generation photovoltaics, especially indoor tandem applications, because they align well with both the solar spectrum and artificial light sources. Quaternary chalcogenides, such as Cu_2ZnSnS_4 (CZTS), offer tunable bandgaps, stability, and earth abundance. In this study, Ag-alloyed CZTS (ACZTS) thin films were synthesized *via* a controlled chemical solution process involving spin coating deposition process and sulfur annealing. Elemental composition and morphology analyses confirmed uniform grain distribution and precise control of the Ag/Cu ratio. Structural characterization *via* X-ray diffraction and Raman spectroscopy revealed a gradual transformation from the kesterite to the stannite phase as the Ag concentration increased. This transformation was accompanied by lattice expansion and a change in crystallite size. Optical measurements showed a clear widening of the bandgap from approximately 1.5 eV of pure CZTS to about 1.7 eV at high Ag levels, supporting its potential use as a top absorber in tandem solar cells. These findings demonstrate that alloying with Ag effectively tailors the properties of CZTS, making it a promising, non-toxic candidate for stable and efficient use in solar cells for indoor environments or high-efficiency tandem applications.

Received 30th September 2025
Accepted 21st October 2025

DOI: 10.1039/d5se01303h

rsc.li/sustainable-energy

Introduction

Kesterite-based semiconductors, such as Cu_2ZnSnS_4 (CZTS) and $Cu_2ZnSnSe_4$ (CZTSe), have gained attention as promising materials for next-generation solar energy harvesting. These materials are a viable alternative to conventional thin-film absorbers like Cu (In, Ga)Se_2 (CIGSe) and CdTe due to their earth-abundant, low-cost, environmentally friendly composition and attractive optoelectronic properties, including a high absorption coefficient and direct tunable bandgap.[1] Most research within this system has focused on selenium-rich compositions, such as CZTSe and CZTSSe. These compositions have relatively narrow band gaps of ~1.0–1.1 eV, making them well-suited for single-junction solar cells. Record efficiencies of up to 15.8% in CZTSSe solar cells have been enabled by continuous progress in deposition methods, band alignment engineering, cationic alloying, and defect control, overcoming nearly a decade of stagnation.[2,3] Although these narrow-bandgap absorbers are well-suited for single-junction solar cells. However, selenium-rich absorbers are not suitable for emerging photovoltaic applications, such as top cell for tandem architectures and indoor (IPVs), which require wider band gaps in the range of 1.6–2.0 eV.[4–6] Pure sulfide CZTS is a more promising candidate because it has a wider band gap of ~1.5 eV which can be tuned to meet these application requirements. Despite having a more favorable bandgap, the record efficiency of pure sulfide CZTS solar cells is limited to 13.2%, which is significantly below the Shockley–Queisser (SQ) limit.[3] This efficiency deficit is attributed to various limitations, including Cu–Zn cation disorder-related defects and the formation of thick interfacial molybdenum disulfide (MoS_2) during growth at the absorber/molybdenum (Mo) back contact, which leads to a defective interface and the growth of small grains.[1,7–9] Therefore, achieving large, continuous grains across the absorber layer while maintaining high electronic quality remains a key challenge in sulfide-based kesterites. Moreover, the ~1.5 eV

[a]*Laboratory of Dosing, Analysis, and Characterisation with High Resolution, Department of Physics, Faculty of Science, Ferhat Abbas University-Setif1, 19000 Setif, Algeria*

[b]*Laboratoire Interdisciplinaire Carnot de Bourgogne (ICB UMR 6303 CNRS), Université de Bourgogne Europe, BP 47 870, 21078 Dijon, France*

[c]*Laboratory of Complex Heterostructures and Multifunctional Materials (HeCoMat), National Institute of Materials Physics, Atomistilor 405A, 077125 Magurele, Romania. E-mail: ac_galca@infim.ro*

[d]*CNRS, Ecole Centrale de Lyon, INSA Lyon, Université Claude Bernard Lyon 1 CPE Lyon, INL, UMR5270, 69100 Villeurbanne, France*

[e]*Laboratory of Surface and Interface Science, National Institute of Materials Physics, Atomistilor 405A, 077125 Magurele, Romania*

[f]*Laboratory of Magnetism and Superconductivity, National Institute of Materials Physics, Atomistilor 405A, 077125 Magurele, Romania*

[g]*International Centre for Advanced Training and Research in Physics, Atomistilor 409, 077125 Magurele, Ilfov, Romania*

bandgap of CZTS, although wider than its Se-rich CZTSSe, still fails to reach the optimal range required for tandem and IPVs applications. This highlights the need for bandgap engineering strategies.

Cationic substitution has emerged as an effective strategy to address the limitations of CZTS and tailor its bandgap for tandem and indoor photovoltaic applications. Substituting Cu^+ with Ag^+, Zn^{2+} with Ba^{2+} or $Sn^{4+}$with Ge^{4+} allows for fine tuning of the lattice parameters, bandgap, and defects.[9–12] W. Gong *et al.* reported bandgap tuning from 1.5 to 2.0 eV in Ag-substituted sulfide CZTS powders.[13] A. Ibrahim *et al.* demonstrated that full substitution of Cu^+ with Ag^+ in Cu_2CdSnS_4 (CCTS) results in a bandgap exceeding 1.9 eV.[14] Beyond Ag substitution, Y. Gong *et al.* demonstrated that substituting Sn^{4+} with Ge^{4+} in CZTS tunes the bandgap from 1.5 to 2.2 eV and promotes the growth of larger grains.[15] Beyond bandgap tuning, Ag incorporation provides significant advantages for kesterite absorbers. Since the ionic radius of Ag^+ (1.14 Å) is much larger than that of Cu^+ (0.74 Å), partial substitution can minimize the formation of Cu–Zn anti-site defects and reduce cationic disorder.[2,16] These improvements have led to better device performance in Se-rich kesterites after nearly a decade of stagnation. Applying this strategy to sulfide-based CZTS is particularly promising because it allows for further bandgap tuning and addresses structural and electronic issues that currently limit device efficiency. Currently, studies on Ag substitution in sulfide-based CZTS are limited. Most previous work focused on bulk powders or solid solutions, and thin film studies primarily focused on low Ag content, which makes the full substitution range unexplored.

This study addresses this knowledge gap by systematically investigating CZTS thin films with Ag substitution across the full Cu/Ag compositional range (0–100%). Molecular ink-based solutions of CZTS, $(Ag, Cu)_2ZnSnS_4$ (ACZTS), and Ag_2ZnSnS_4 (AZTS) were synthesized, deposited by spin coating, and subsequently subjected to sulfurization annealing. A comprehensive set of characterization techniques, including X-ray diffraction (XRD), Raman spectroscopy, scanning electron microscopy (SEM) with energy-dispersive X-ray spectroscopy (EDS), X-ray photoelectron spectroscopy (XPS), and diffuse reflectance spectroscopy, was employed to evaluate the structural, morphological, optical, and electronic properties. This work provides fundamental insights into the role of Ag substitution in sulfide kesterites through the analysis of these properties across the full substitution range and supports the development of wide-bandgap absorbers for tandem and IPVs applications.

Experimental section

Fabrication of Ag-alloyed CZTS absorber layers

Silver alloyed Cu_2ZnSnS_4 (CZTS) thin films were prepared using the spin coating of a molecular ink. The precursor materials included copper(II) acetate monohydrate ($Cu(CH_3COO)_2 \cdot H_2O$), zinc acetate dihydrate ($Zn(CH_3COO)_2 \cdot 2H_2O$), tin(II) chloride ($SnCl_2 \cdot 2H_2O$), thiourea ($CS(NH_2)_2$) and silver nitrate ($AgNO_3$). 2-Methoxyethanol (MOE) was used as the solvent. The precursor solution was prepared through a two-step process. First, $AgNO_3$, Zn $(CH_3COO)_2 \cdot 2H_2O$ and $CS(NH2)_2$ were dissolved in MOE. Separately, Cu $(CH_3COO)_2$ and $SnCl_2 \cdot 2H_2O$ were also dissolved in MOE. Subsequently, the two solutions were combined and stirred at room temperature for 2 hours to achieve a homogeneous mixture.

To study the effect of silver alloying, eight precursor solutions were prepared with different Ag/(Ag + Cu) molar ratios: 0%, 2%, 5%, 10%, 25%, 50%, 75%, and 100%. The precise chemical concentrations used for each composition are summarized in Table 1.

Thin films were deposited by spin coating on molybdenum-coated soda-lime glass (SLG/SiO_2/Mo) substrates. The spin coating parameters were set at 3000 rpm for 30 seconds, followed by drying on a hot plate at 280 °C for 3 minutes. To achieve the desired film thickness, this cycle was repeated five times. After deposition, the films were heat-treated in a tubular furnace under an argon atmosphere. The annealing was performed at 580 °C for 15 minutes at a heating rate of 10 °C min^{-1}. To overcome the loss of sulfur during the heat treatment, the samples were placed in a graphite box containing 0.1 g of sulfur flakes. After annealing, the samples were naturally cooled to room temperature.

Characterizations

The structural characterization of the $(Ag, Cu)_2ZnSnS_4$ (ACZTS) thin films was performed by X-ray diffraction using an Anton Paar XRDynamic 500 instrument. The measurements were performed using Cu Kα radiation source ($\lambda_{K\alpha_1} = 1.5406$ Å, $\lambda_{K\alpha_1} = 1.5444$ Å) with a step width of 0.02° and a counting time of 1 s

Table 1 Precursor concentrations for CZTS solution preparation with different Ag substitution concentration

Concentration (mol L^{-1})	$AgNO_3$	$CS(NH_2)_2$	$Zn(CH_3COO)_2$	$SnCl_2$	$Cu(CH_3COO)_2$
CZTS-0Ag	—	2.64	0.437	0.49	0.84
CZTS-2Ag	0.0168	2.64	0.437	0.49	0.823
CZTS-5Ag	0.042	2.64	0.437	0.49	0.798
CZTS-10Ag	0.084	2.64	0.437	0.49	0.756
CZTS-25Ag	0.21	2.64	0.437	0.49	0.63
CZTS-50Ag	0.42	2.64	0.437	0.49	0.42
CZTS-75Ag	0.63	2.64	0.437	0.49	0.21
CZTS-100Ag	0.84	2.64	0.437	0.49	—

per step, over a 2θ range from 10° to 60°. Raman spectroscopy (Horiba Jobin-Yvon) was employed to check the microstructure and to look for possible secondary phases using two excitation wavelengths (633 nm and 325 nm). Morphological characterization and chemical composition were analyzed using a field emission scanning electron microscope (FESEM) Zeiss Gemini 500 equipped with a Bruker energy dispersive X-ray (EDX) analyzer. The surface of the films was characterised by X-ray photoelectron spectroscopy (XPS) using a monochromatized Al Kα source at 1486.6 eV and a power of 144 W (12 kV × 12 mA), employing a Kratos Axis Ultra spectrometer. The analyzer was operated in fixed analyzer transmission (FAT) mode, and high-resolution spectra were acquired at 20 eV pass energy and 0.05 eV energy step. Surface charging effects were compensated by using an electron flood gun during measurement and by later correcting the C–C contamination bond at 284.8 eV. The optical properties of the films were investigated using a spectrophotometer equipped with an integrating sphere to collect the diffuse reflectance spectra.

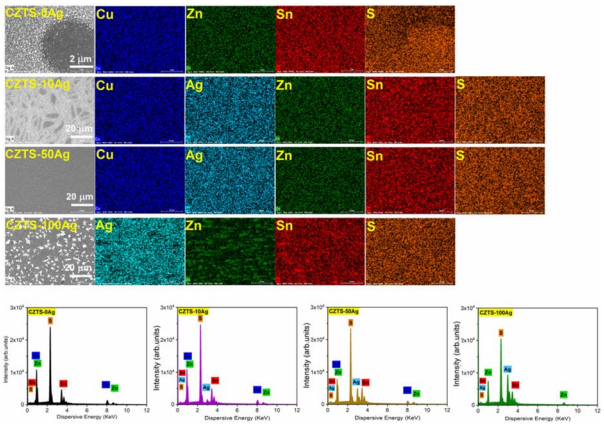

Fig. 1 EDX mapping images for Ag, Cu, Zn, Sn and S, Obtained from CZTS, ACZTS and AZTS samples.

Results and discussion

Morphological properties

Energy dispersive X-ray spectroscopy (EDX) and elemental mapping of $(Ag, Cu)_2ZnSnS_4$ (ACZTS) films (Fig. 1) confirm the homogeneous distribution of Ag, Cu, Zn, Sn, and S across all silver incorporation levels. The spatially resolved analysis demonstrates uniform substitution of Ag for Cu in the kesterite lattice without detectable phase segregation or secondary phase formation. Critically, stoichiometric Zn/Sn ratios and consistent sulfur distribution are maintained regardless of Ag content, indicating effective suppression of S-vacancies and Sn-related defects during synthesis. This compositional homogeneity, validated across multiple Ag proportions, establishes a defect-suppressed absorber foundation essential for enhanced photovoltaic performance in Ag-alloyed kesterites.

The compositional evolution of $Ag_xCu_{2-x}ZnSnS_4$ ($(Ag, Cu)_2ZnSnS_4$) films with increasing Ag/(Ag + Cu) molar ration (0–100%) reveals two distinct regimes (Fig. 2). Below 50% Ag/(Ag + Cu), The Cu content gradually decreased with increasing Ag incorporation, while Zn (~10%), Sn (~12.5%), and S (~58%) maintain strict stoichiometry, suggesting isovalent substitution of Ag^+ for Cu^+ without disrupting cation–anion balance. Correspondingly, the (Ag + Cu)/(Zn + Sn) ratio remains near-ideal (0.89–0.96, Table S1), validating phase-pure kesterite formation where Ag alloying suppresses Cu_{Zn} antisites while preserving charge neutrality.

Beyond 50% Ag/(Ag + Cu), however, thermodynamic instability emerges Zn content rises sharply to 14.2% at 100% Ag/(Ag + Cu) concentration, depressing the (Ag + Cu)/(Zn + Sn) ratio to 0.80, which is significantly below the optimal kesterite range (0.85–1.10), and elevating Zn/Sn ratio by >40%. This deviation consists with attenuated Sn and S stability, and suggests the onset of Zn-rich secondary phase formation, most likely ZnS.

The Ag/(Ag + Cu) atomic ratios in ACZTS films exhibit near-perfect linearity with designed values across all concentrations, demonstrating unprecedented compositional fidelity in solution-processed multinary chalcogenides.

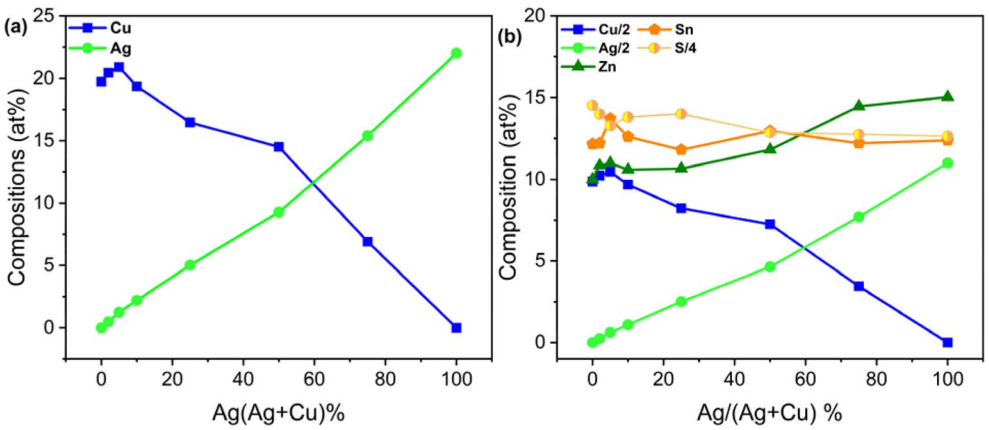

Fig. 2 (a) Composition ratio of Cu and Ag in samples with different Ag substitution concentrations, (b) composition ration of all elements in CZTS with different Ag doping levels.

This compositional precision enables targeted material design: Controlled Ag substitution (<50%) optimizes defect thermodynamics for enhanced carrier lifetime, while Zn enrichment at higher concentrations provides diagnostic markers for recombination-active interfacial phases.

Fig. 3 reveals the profound impact of Ag substitution on the morphology of ACZTS films, establishing a critical composition–structure–property relationship. Ag-free films exhibit surfaces with a high defect density characterized by irregular nano-grains (50–100 nm) with pervasive micro-cracks (Fig. 3a, 0% Ag/(Ag + Cu)), consistent with inefficient carrier transport in pristine CZTS. Low Ag incorporation (2–10% Ag/(Ag + Cu)) induces modest grain growth (150–200 nm) but retains crack networks and void densities >15% (Fig. 3a, 2–10%), leading to a limited photovoltaic improvement at these concentrations. The cross-sectional SEM images (Fig. 3b) confirm these observations, showing discontinuous grain columns and vertical cracks are most likely linked to interfacial instability during the sulfurization process. At high temperatures a thick MoS_2 interlayer can form at the Mo/absorber interface, leading to decomposition of CZTS phase according to the following reaction: $2Cu_2ZnSnS_4 + Mo \rightarrow 2Cu_2S + 2ZnS + 2SnS + MoS_2$. The Gibbs free energy of this reaction has been calculated to be −150 kJ for CZTS at 550 °C.[17] This indicates that the decomposition of CZTS in contact with Mo is thermodynamically favorable and that the CZTS/Mo interface becomes unstable during high-temperature processing. This instability can generate voids and weak adhesion at the back contact. Under thermal stress, this can lead to the propagation of vertical cracks, as observed in the 0–10% Ag samples. A distinct morphological transition occurs at 25% Ag/(Ag + Cu): the surface evolves into a compact, pinhole-free microstructure with homogeneous, columnar grains (300–400 nm) and crack suppression. This suggests that Ag incorporation alters the defect chemistry and stabilizes the kesterite lattice, making the interface less susceptible to MoS_2-induced decomposition (Fig. 3a and b, 25%). Beyond this concentration, 50–75% Ag/(Ag + Cu) incorporation leads to unfavorable phase separation. This is manifested by larger, yet incoherent, grains (500–700 nm), reappearance of intergranular voids, and reduced density (Fig. 3a and b, 50–75%). Cross-sectional images confirm the vertical grain alignment disorder and porous region reappearance, consistent with reduced film quality. At 100% Ag/(Ag + Cu), micron-sized grains with enhanced compactness are formed (Fig. 3a and b, 100%).

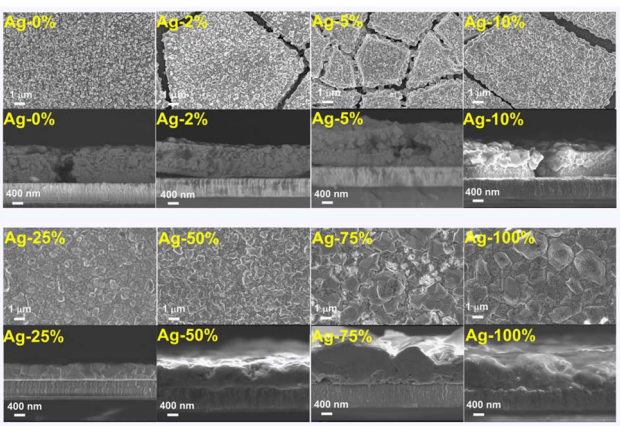

Fig. 3 Scanning Electron Microscope (SEM) top-view and cross-sectional images of CZTS with different Ag doping levels.

Structural properties

X-ray diffraction and Raman spectroscopy have been used to study the structural evolution of (Ag, Cu)$_2$ZnSnS$_4$ (ACZTS) thin films with different Ag/(Ag + Cu) ratios. XRD analysis provides information on phase identification, peak shifts and lattice parameter variations, while Raman spectroscopy confirms the phase composition and detects possible secondary phases. The use of two Raman excitation wavelengths (633 nm and 325 nm) allows comprehensive characterization.

X-ray diffraction (XRD)

The XRD patterns of the ACZTS films with different silver incorporations are shown in Fig. 4. For Ag concentrations from 0% to 50% Ag/(Ag + Cu), the diffraction peaks corresponding to 101, 110, 112, 200, 220/204, and 312/116 crystallographic reflections, which can be attributed to the tetragonal Cu2ZnSnS4 (ICDD #01-084-8523). The most intense peak 112 shifts progressively from 28.46° (0% Ag/(Ag + Cu)) to 28.16° (50% Ag/(Ag + Cu)), suggesting the isovalent substitution with larger Ag+ ions (1.14 Å) of Cu (0.74 Å), inducing therefore lattice expansion that should follow Vegard's law (Fig. 4b).

At 50% Ag/(Ag + Cu), phase coexistence emerges, while 112 peak persists at 28.16°, a new reflection, confirming complete Cu → Ag substitution.[18] The diffraction peak of the Mo substrate is observed ($2\theta = 40.46$, peaks corresponding to the 110 reflection, ICDD #04-014-7435), and no other secondary phases ZnS (ICDD #04-008-7254), SnS (ICDD #00-053-0526), or Ag_2S (ICDD #04-027-0784) were detected within the measurement limits, validating the synthesis approach efficacy in suppressing recombination-active impurities. This phase-pure transition below 50% Ag/(Ag + Cu) provides the structural foundation for enhanced photovoltaic performance in Ag-alloyed kesterites.

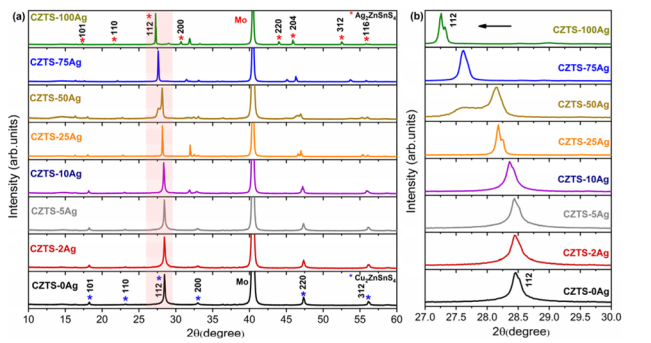

Fig. 4 (a) The X-ray diffraction (XRD) of films Mo/ACZTS with different Ag doping, (b) enlarged view of the 112 diffraction peaks with different Ag doping.

Structural parameters of ACZTS films were derived from XRD patterns using Braggs law (eqn (1))

$$n\lambda = 2d\sin(\theta) \quad (1)$$

where n is an integer, λ is the X-ray wavelength (1.5406 Å for Cu Kα), d is the interplanar spacing, and θ is the diffraction angle.[19] For a tetragonal crystal structure, the lattice parameters a and c were calculated from two major diffraction peaks using the relation (eqn (2)):

$$\frac{1}{d^2} = \frac{h^2 + k^2}{a^2} + \frac{l^2}{c^2} \quad (2)$$

The subscript hkl of the interplanar spacing d refers to the Miller indices of the crystallographic plane.

As quantified in Table S2, progressive Ag incorporation (0–50%) expands the lattice constant a, from 5.427 Å to 5.512 Å, consistent with isovalent substitution of smaller Cu^+ (0.74 Å) by larger Ag^+ (1.14 Å).[13] In contrast, the lattice parameter c remains invariant (10.84–10.86 Å) within this composition range, indicating anisotropic lattice relaxation. Above 50% Ag/(Ag + Cu), a structural phase transition emerges, namely, c contracts significantly (to 10.72 Å at 100% Ag/(Ag + Cu)), while a continues expanding (to 5.632 Å). This distortion is quantified by the $c/2a$ ratio (Fig. 5), which decreases by 8.2% between 50–100% Ag/(Ag + Cu)-possibly due to tetragonal kesterite (space group $I\bar{4}$) to tetragonal stannite ($I\bar{4}2m$) phase transformation.[18] This structural evolution aligns with Cu_2(Zn, Mn)$SnSe_4$ and Cu_2(Zn, Fe)SnS_4, supporting the universal behavior in Cu_2-based chalcogenides.[20,21]

The crystalline volume ($V = a^2c$) increases by 4.3% at 50% Ag/(Ag + Cu) (compared to pristine CZTS), driven solely by an a-axis expansion. While despite c-axis contraction above 50% Ag/(Ag + Cu), V rises another 2.1% due to continue a-axis growth, reflecting irreversible reorganization during phase transition. The absence of secondary phase peaks (ZnS, SnS, Ag_2S) confirms that these volume changes result from intrinsic cation substitution, rather than the formation of impurity phases.

The average crystallite size of ACZTS thin films with varying Ag/(Ag + Cu) molar ration was calculated using the Scherrer equation (eqn (3)), based on the full width at half maximum (FWHM) of the dominant diffraction peaks (Table S3).[22]

$$D_{hkl} = \frac{K\lambda}{\mathrm{FWHM}\cdot\cos\theta_{hkl}} \quad (3)$$

where D is the average crystallite size (nm), k dimensionless shape factor with a value (~0.9), λ is the X-ray wavelength (CuKα = 1.5406 Å), θ is the Bragg's angle.

At low Ag concentrations (0–10% Ag/(Ag + Cu)) the crystallite size remained constrained to 18–22 nm, reflecting suppressed grain growth despite Ag incorporation. This aligns with SEM observations of irregular nanoscale grains and persistent microcracks, indicating limited atomic mobility during film crystallization. A transformative shift occurs at 25% Ag/(Ag + Cu) substitution, where crystallite sizes increase significantly by >150% (to 45–55 nm across multiple [hkl] direction). This abrupt corresponds to a significant improvement in surface morphology where the films become more compact and homogeneous, suggesting improved crystallinity and structural ordering. At 50–75% Ag/(Ag + Cu), kesterite–stannite phase coexistence drives severe crystallographic fragmentation, reducing [112]-oriented crystallite dimensions to 36 ± 4 nm while inducing preferential [001] texturing. This anisotropic restructuring, quantified by a 32% increase in [001]/[112] intensity ratio, accommodates transformation strain through crystallographic shear planes, generating intra-grain point defects that significantly affect the optoelectrical properties of the absorber.

At 100% Ag/(Ag + Cu), complete transformation to the tetragonal stannite phase drives recrystallization into micron-scale stannite domains (102 ± 8 nm) with high-angle grain boundaries that exhibit elemental segregation of Sn and Ag.

These results confirm that Ag incorporation significantly affects the crystalline structure and morphology of ACZTS films. It also leads to lattice expansion, as reflected by the calculated lattice parameters and the evolution of crystallite size. These structural modifications play a critical role in the phase transformation and film quality.

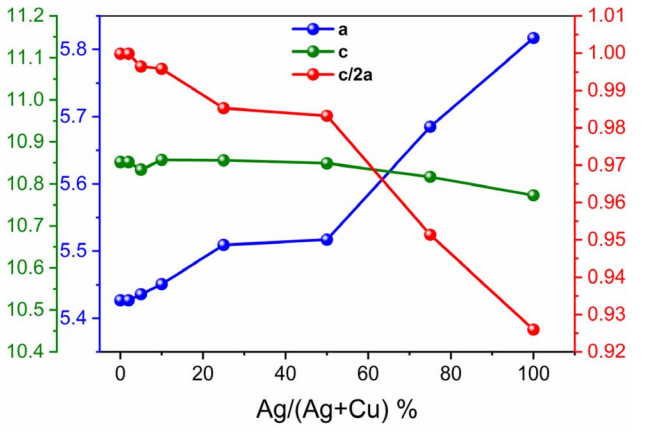

Fig. 5 Lattice parameters a, c and $c/2a$ with different Ag substitution concentrations (Ag/Ag + Cu).

Raman spectroscopy

The Raman spectra of ACZTS thin films with varying Ag/(Ag + Cu) molar ratios are presented in Fig. 6 and 7. These were acquired using two excitation wavelengths: 633 nm (visible range) and 325 nm (UV range), respectively.

With 633 nm excitation and a 25% neutral density (ND) filter (Fig. 6a), the dominant vibrational mode shifts progressively as the Ag content increases. For films with Ag/(Ag + Cu) ratios of 0%, 2%, 5%, 10%, 25% and 50%, the most intense peak appears between 329.9 cm^{-1} and 332.8 cm^{-1}. Although no secondary phases were detected under these conditions, identification of the kesterite phase cannot be conclusively confirmed due to lower Raman shift values than those typically reported in the literature.[16,23,24] These lower values may result from reduced spectral resolution and local heating effects at higher laser power.

At 75% Ag/(Ag + Cu), a new peak appears at 335.1 cm^{-1}, accompanied by a weaker feature at ~274 cm^{-1}. This suggests

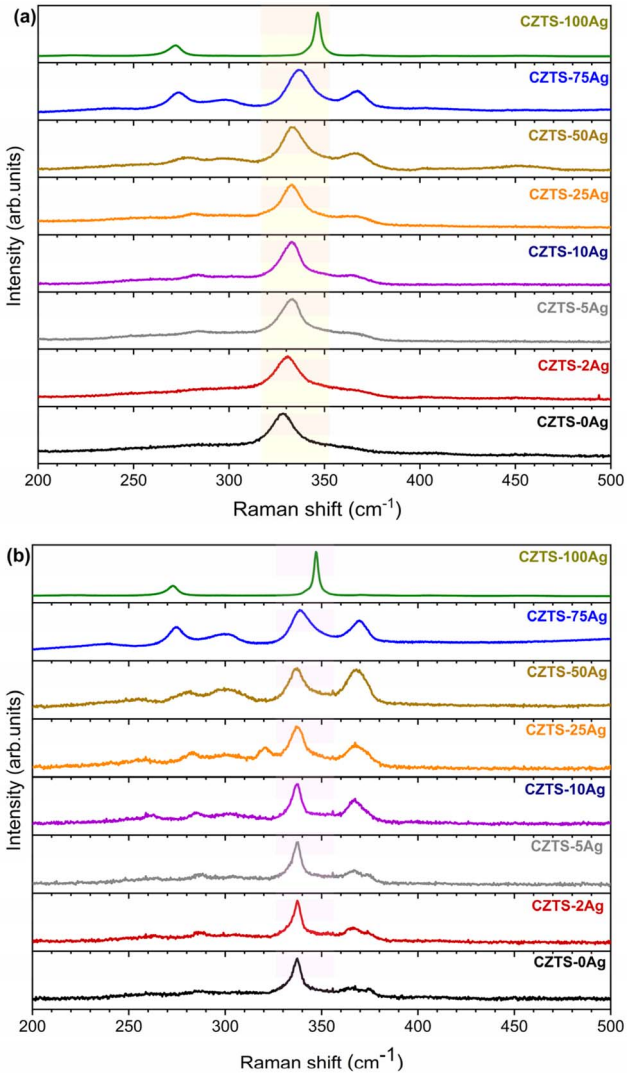

Fig. 6 Raman spectra of Ag-alloyed CZTS absorber layers under 633 nm excitation using tow laser intensities: (a) 25% ND filter and (b) 3.2% ND filter.

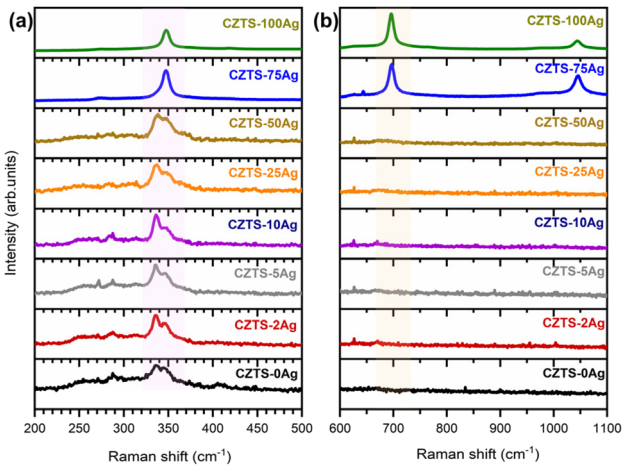

Fig. 7 Raman spectra of Ag-alloyed CZTS absorber layers under 325 nm excitation (a and b).

a degree of structural rearrangement and the onset of a phase transition. The Raman spectrum shows two characteristic peaks at 346.4 cm^{-1} (A1 mode) and 272 cm^{-1} (E mode) when the Ag/(Ag + Cu) is at 100%, confirming the formation of the stannite phase Ag_2ZnSnS_4 (AZTS).[18] This is consistent with the XRD results.

To improve spectral resolution and obtain more reliable peak positions, Raman measurements were repeated using a 3.2% ND filter to correspond to lower laser intensity and reduced thermal effects. Under these conditions, the main Raman peaks for samples containing 0–50% Ag/(Ag + Cu) were consistently located at ~337 cm^{-1} (A_1 mode) and ~366–367 cm^{-1}, which is in good agreement with the kesterite structure. The 25% Ag sample exhibited peaks at 336.7 cm^{-1} (A_1) and 367.3 cm^{-1}, while the 50% Ag sample showed modes at 300 cm^{-1}, 337.3 cm^{-1} (A_1), and 368 cm^{-1}. The 75% Ag sample showed a slight blueshift to 338.7 cm^{-1}, along with additional features at ~274 cm^{-1} and 369.6 cm^{-1}, which were still within the expected range for strained or alloyed kesterite structures.[23–27]

The dominant peak shifts to 347 cm^{-1} and the E-mode shifts to around 272 cm^{-1} at 100% Ag/(Ag + Cu), where a clear spectral evolution is observed. Both of these are consistent with the stannite-type AZTS phase. These results confirm the complete structural transition from kesterite to stannite, as indicated by XRD and lattice parameter analysis.[18]

The slight Raman peak shifts seen between the ND 25% and ND 3.2% filter measurements are attributed to laser-induced local heating at higher power.[27] This thermal effect is more pronounced in partially Ag-substituted films (0–75% Ag), which are structurally less stable. In contrast, the 100% Ag sample, corresponding to the stannite phase, shows minimal shift, indicating its higher thermal and structural stability under laser excitation.

To further probe the presence of secondary phases, UV Raman spectroscopy was performed using a 325 nm excitation wavelength, which is inherently surface sensitive due to its shorter optical penetration depth. For Ag alloying levels up to 50%, extraneous vibrational modes were observed, confirming the structural purity of the CZTS phase across this composition range. At higher Ag concentrations (≥75%), distinct additional peaks appeared at 347.8 cm^{-1}, 697.2 cm^{-1} (2LO), and 1045 cm^{-1}(3LO), corresponding to the characteristic longitudinal optical phonon modes of ZnS.[28] These results are in agreement with the EDX analysis which revealed a notable increase in Zn content (up to 14.2 at 100% Ag) and with SEM observations of surface degradation at high Ag incorporation. The correlation between Zn enrichment and the emergence of ZnS vibrational signatures strongly suggests phase segregation at elevated Ag/(Ag + Cu) ratios.

Importantly, the absence of Raman signatures from common secondary phases such as SnS (160–220 cm^{-1}) and Cu_2S (approximately at 475 cm^{-1}) below 50% Ag underscores the compositional threshold for maintaining phase-pure kesterite, a prerequisite for achieving optimal photovoltaic performance.[29–32]

Oxidation states and electronic structure transition

X-ray photoelectron spectroscopy (XPS) analysis of the ACZTS samples reveals a systematic evolution in oxidation states and electronic structure as Ag gradually replaces Cu in the lattice (Fig. 8). The Ag $3d_{5/2}$ peaks appear between 367.8 eV and 368.1 eV, corresponding to Ag^{+}.[33] The Cu $2p_{3/2}$ peaks appear between 931.7 eV and 932.0 eV, characteristic of Cu^{+} species, with no satellite's indicative of Cu^{2+}.[34,35] Considering that the samples were exposed to air before *in situ* measurement, and giving that copper instantly oxidizes, we can state the surface is Cu deficient, and that the structures end in Sn, since mainly in Sn 3d spectra we see Sn–O bonds. Up to 75% Ag/(Ag + Cu) content, the Zn $2p_{3/2}$ (1021.4–1021.7 eV) and Sn $3d_{5/2}$ (486.25–486.4 eV) binding energies remain nearly invariant, indicating preserved Zn^{2+}–S and Sn^{4+}–S coordination consistent with a stable kesterite lattice, as corroborated by XRD analysis.[33,35] At full Ag substitution (100% Ag/(Ag + Cu)), distinct core-level shifts are observed: Zn $2p_{3/2}$ shifts +0.7 eV (to 1022.1 eV) and Sn $3d_{5/2}$ increases +0.9 eV (to 487.3 eV).[33] These concurrent shifts signal enhanced Sn 5s–Zn 3d orbital hybridization during the kesterite-to-stannite phase transition, wherein Sn relocates from tetrahedral to more distorted octahedral coordination environments.[33] The S 2p signal comes from the (161.5–162.0 eV) S^{2-} species, with minor surface contributions from elemental sulfur and oxidized species,[33,34] and since in this technique, the chalcogens exhibit similar energies, a distinction between bonds is not possible. However, the different signatures are distinguishable in the valence band spectra, providing information on the electronic reconfiguration.[22] At low Ag content (<10%), the valence band maximum (VBM) remains poorly defined, which may be due to a high degree of disorder and localized states, consistent with Fermi level pinning by deep level Cu_{Zn}–Sn_{Zn} antisite defect complexes. At 25% Ag/(Ag + Cu), the VBM becomes sharply defined and shifts toward higher binding energies with Ag incorporation. This transition indicates a shift from significantly p-type (p+) to moderately p-type conductivity, characterized by a decrease in hole concentration.

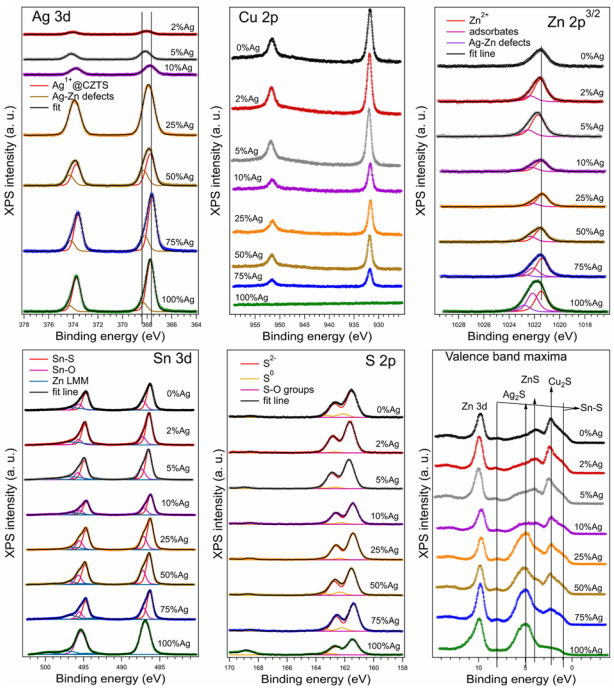

Fig. 8 XPS spectra of CZTS absorber layers with different concentrations of silver: Cu 2p, Ag 3d, Zn 2p3/2, Sn 3d and S 2p.

Optical properties

The optical band gap (E_g) of ACZTS films with different Ag content (0%, 2%, 5%, 10%, 25%, 50%, 75% and 100% Ag/(Ag + Cu)) was determined by diffuse reflectance spectroscopy. The Kubelka–Munk $F(R)$ function defined as (eqn (4)):

$$F(R) = \frac{(1-R)^2}{2R} \tag{4}$$

was employed to convert the reflectance data into absorption equivalent spectra. R is the diffuse reflectance, k is the extinction coefficient, and s is the scattering coefficient.[36,37] The optical band gap of the samples was obtained by extrapolation the linear region of the $[F(R)\cdot h\nu]^2$ function, which is equivalent to Tauc plot, as a function of photon energy, E (eV).

The E_g values of the ACZTS films as function of varying Ag concentrations are presented in Fig. 9. The band gap of pure CZTS is measured at around 1.52 eV, which is consistent with values reported in the literature. No significant increase in the band gap is observed with 2% Ag/(Ag + Cu) incorporation, and it remains within the range of 1.53 eV to 1.59 eV for 5% Ag/(Ag + Cu). However, for Ag concentrations above 10% the band gap increases, ranging from 1.60 eV to 1.71 eV as the Ag content increases. The variation of E_g with Ag/(Ag + Cu) ratio is clearly non-linear. This behavior reflects the competition between Ag-induced lattice expansion and the evolution of intrinsic defects and secondary phases. At low Ag content (<10%), residual Cu–Zn antisite disorder pins the band edges and suppresses bandgap widening. From about 25% Ag onward, the larger Ag^{+} ionic radius reduces antisite defects and promotes a more ordered kesterite lattice, producing the pronounced increase in E_g (~1.7 eV). At very high Ag levels (≥75%), the emergence of stannite domains and ZnS-rich segregations, evidenced by UV-Raman and EDX, introduces localized electronic states that partially offset the Ag-induced widening. The net result is a deviation from a simple Vegard-type linear dependence of E_g on composition. This tunable band gap

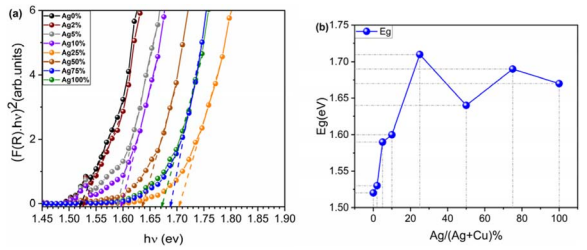

Fig. 9 (a) Kubelka–Munk transformed $(F(R)\cdot h\nu)^2$ variation with photon energy (eV), and (b) the corresponding band gap values for ACZTS films with different silver (Ag) incorporation.

broadening enhanced the suitability of ACZTS films for advanced optoelectronic applications including tandem solar cell integration and low-intensity indoor photovoltaic.

Conclusions

This study reports the successful synthesis of (Ag, Cu)$_2$ZnSnS$_2$ (ACZTS) thin films *via* a scalable and controllable chemical solution process. This method facilitated precise fine-tuning of the Ag/(Ag + Cu) molar ratio, thereby enabling optimal control over the film properties. A structural analysis was conducted, which revealed a gradual shift from a kesterite phase to a stannite phase with increasing Ag content. This transformation was accompanied by lattice expansion and a change in the crystallite size.

The XPS results indicate successful formation of the desired chemical environment, with the presence of Ag^+ and Cu^+ ions in the crystal structure, suggesting that Ag^+ substitution for Cu^+ is occurring. Consequently, a slight downward shift in the valence position was observed, which is a critical factor in achieving optimal doping level and band alignment in thin films solar cells. The Ag led to significant bandgap expansion, from 1.52 eV for the pure CZTS to 1.68–1.71 eV for high Ag alloys. This incorporation approach is particularly promising for absorber engineering, making it suitable for new applications, such as tandem and indoor photovoltaics.

This work highlights the potential of chemical solution deposition as an efficient, cost-effective approach for engineering multi-cation chalcogenide thin films with fine-tuned chemical compositions as well as structural, electronic, and optical properties.

Author contributions

M. T: conceptualization; investigation; methodology; formal analysis; visualization writing – original draft; O. E. K: methodology; investigation; formal analysis; visualization; supervision; writing – review & editing. M. G: funding acquisition; supervision; validation; writing – review & editing. C. T: conceptualization, validation; supervision; formal analysis; writing – review & editing. A. E. B: investigation; formal analysis; visualisation; validation; writing – original draft. I. A: investigation; formal analysis; visualisation; validation; writing – original draft. D. C: project administration; supervision; validation; writing – review & editing. A. C. G: conceptualization; investigation; formal analysis; resources; project administration; funding acquisition; validation; supervision; writing – original draft; writing – review & editing.

Conflicts of interest

There are no conflicts to declare.

Data availability

The datasets generated during and/or analyzed during the current study are available from the authors on reasonable request.

Supplementary information is available. See DOI: **https://doi.org/10.1039/d5se01303h**.

Acknowledgements

M. T. and M. G. acknowledge the financial support from the Algerian Ministry of Higher Education and Scientific Research (MESRS). M. T. acknowledges the receipt of the AF-106_25_01 grant financed by Abdus Salam International Centre for Theoretical Physics, Trieste, Italy, from the Centre International de Formation et de Recherche Avancées en Physique, subsidiary of National Institute of Materials Physics, Magurele, Romania. M. T. acknowledges the Romanian Ministry of Foreign Affairs and the Agence Universitaire de la Francophonie for the Eugen Ionescu research and mobility grant at the National Institute of Materials Physics. Authors acknowledge the COST Action Research and International Networking project "Emerging Inorganic Chalcogenides for Photovoltaics (RENEW-PV)", CA21148, supported by COST (European Cooperation in Science and Technology). NIMP authors acknowledge funding from Autoritatea Națională pentru Cercetare (Romanian National Authority for Research) through the Core Programme PC3-PN23080303 project, and from Unitatea Executivă pentru Finanțarea ÎnvățământuluiSuperior, a Cercetării, Dezvoltării și Inovării (UEFISCDI) through ERANET-M-3-ERANET-Ligthcell (Contract No. 19/15.03.2024) project. The XPS measurements were performed using the Romanian National Interest Setup "System of complex XPS/ESCA installations and research using synchrotron radiation".

References

1 X. Liu, Y. Feng, H. Cui, G. Conibeer, D. B. Mitzi and M. Green, The current status and future prospects of kesterite solar cells: a brief review, *Prog. Photovoltaics*, 2016, **24**, 879–898, DOI: **10.1002/pip.2741**.

2 J. Zhou, X. Xu, H. Wu, J. Wang, L. Lou, K. Yin, Y. Gong, J. Shi, Y. Luo, D. Li, H. Xin and Q. Meng, Control of the phase evolution of kesterite by tuning of the selenium partial pressure for solar cells with 13.8% certified efficiency, *Nat. Energy*, 2023, **8**, 526–535, DOI: **10.1038/s41560-023-01251-6**.

3 M. A. Green, E. D. Dunlop, M. Yoshita, N. Kopidakis, K. Bothe, G. Siefer, X. Hao and J. Y. Jiang, Solar Cell Efficiency Tables (Version 66), *Prog. Photovoltaics*, 2025, **33**, 795–810, DOI: **10.1002/pip.3919**.

4 A. Chakraborty, G. Lucarelli, J. Xu, Z. Skafi, S Castro-Hermosa, A. B. Kaveramma, R. G. Balakrishna and T. M. Brown, Photovoltaics for indoor energy harvesting, *Nano Energy*, 2024, **128**, 109932, DOI: **10.1016/j.nanoen.2024.109932**.

5 T. Kirchartz and U. Rau, What Makes a Good Solar Cell?, *Adv. Energy Mater.*, 2018, **8**, 1703385, DOI: 10.1002/aenm.201703385.

6 M. He, M. Zhang, Z. Li, X. Liu, K. Sun, Z. Liu and X. Hao, Top Cells for Silicon-Based Tandem Photovoltaics, *Adv. Mater.*, 2025, **37**(40), 2411858, DOI: 10.1002/adma.202411858.

7 A. Wang, J. Cong, S. Zhou, J. Huang, J. Cao, X. Cui, X. Yuan, Y. Yao, Z. Xu, G. He, J. Z. Liu, J. M. Cairney, Y. Chen, M. A. Green, S.-H. Wei, K. Sun and X. Hao, Hydrogen-Enhanced Carrier Collection Enabling Wide-Bandgap Cd-Free Cu_2ZnSnS_4 Solar Cells with 11.4% Certified Efficiency, *Nat. Energy*, 2025, **10**(2), 255–265, DOI: 10.1038/s41560-024-01694-5.

8 A. Wang, J. Huang, J. Cong, X. Yuan, M. He, J. Li, C. Yan, X. Cui, N. Song, S. Zhou, M. A. Green, K. Sun and X. Hao, Cd-Free Pure Sulfide Kesterite Cu_2ZnSnS_4 Solar Cell with Over 800 mV Open-Circuit Voltage Enabled by Phase Evolution Intervention, *Adv. Mater.*, 2024, **36**(3), 2307733, DOI: 10.1002/adma.202307733.

9 J. Li, D. Wang, X. li, Y. Zeng and Y. Zhang, Cation Substitution in Earth-Abundant Kesterite Photovoltaic Materials, *Adv. Sci.*, 2018, **5**(4), 1700744, DOI: 10.1002/advs.201700744.

10 Y. Kim, H. Hempel, S. P. Harvey, N. A. Rivera, T. Unold and D. B. Mitzi, Alkali Element (Li, Na, K, and Rb) Doping for $Cu_2BaGe_{1-x}Sn_xSe_4$ Films, *J. Mater. Chem. A*, 2023, **11**, 15336–15346, DOI: 10.1039/D3TA01494K.

11 T. Gershon, Y. S. Lee, P. Antunez, R. Mankad, S. Singh, D. Bishop, O. Gunawan, M. Hopstaken and R. Haight, Photovoltaic Materials and Devices Based on the Alloyed Kesterite Absorber $(Ag_xCu_{1-x})2ZnSnSe_4$, *Adv. Energy Mater.*, 2016, **6**(10), 1502468, DOI: 10.1002/aenm.201502468.

12 A. Walsh, S.-H. Wei, S. Chen and X. G. Gong, Design of quaternary chalcogenide photovoltaic absorbers through cation mutation, *2009 34th IEEE Photovoltaic Specialists Conference (PVSC)*, Philadelphia, PA, USA, 2009, pp. 001875–001878, DOI: 10.1109/PVSC.2009.5411555.

13 W. Gong, T. Tabata, K. Takei, M. Morihama, T. Maeda and T. Wada, Crystallographic and optical properties of $(Cu, Ag)_2ZnSnS_4$ and $(Cu, Ag)_2ZnSnSe_4$ solid solutions, *Phys. Status Solidi C*, 2015, **12**(6), 700–703, DOI: 10.1002/pssc.201400343.

14 A. Ibrahim, S. Lie, J. M. R. Tan, R. Swope, A. G. Medaille, S. Hadke, E. Saucedo, R. Agrawl and L. H. Wong, Efficiency enhancement and doping type inversion in Cu_2CdSnS_4 solar cells by Ag substitution, *J. Mater. Chem. A*, 2024, **12**, 2673–2679, DOI: 10.1039/D3TA04529C.

15 Y. Gong, O. El Khouja, A. Jimenez-Arguijo, I. Caño, H. Goniotakis, A. Navarro-Güell, O. Segura-Blanch, M. Dimitrievska, C. Malerba, M. Valentini, S. Giraldo, M. Placidi, Z. Jehl Li-Kao and E. Saucedo, Over 18% Efficient Cu_2ZnSnS_4 Solar Cells for Indoor Photovoltaics: Unlocking the New Potential of Kesterite Technology, *NEXTGEN 2025*, Mallorca, Spain, 2025.

16 Y. Gong, R. Qiu, C. Niu, J. Fu, E. Jedlicka, R. Gridharagopal, Q. Zhu, Y. Zhou, W. Yan, S. Yu, J. Jiang, S. Wu, D. S. Ginger, W. Huang and H. Xin, Ag Incorporation with Controlled Grain Growth Enables 12.5% Efficient Kesterite Solar Cell with Open Circuit Voltage Reached 64.2% Shockley–Queisser Limit, *Adv. Funct. Mater.*, 2021, **31**(24), 2101927, DOI: 10.1002/adfm.202101927.

17 J. J. Scragg, T. Kubart, J. T. Wätjen, T. Ericson, M. K. Linnarsson and C. Platzer-Björkman, Effects of Back Contact Instability on Cu 2 ZnSnS 4 Devices and Processes, *Chem. Mater.*, 2013, **25**(15), 3162–3171, DOI: 10.1021/cm4015223.

18 K. Pietak, C. Jastrzebski, K. Zberecki, D. J. Jastrzebski, W. Paszkowicz and S. Podsiadlo, Synthesis and structural characterization of Ag2ZnSnS4 crystals, *J. Solid State Chem.*, 2020, **290**, 121467, DOI: 10.1016/j.jssc.2020.121467.

19 G. F. Harrington and J. Santiso, Back-to-Basics tutorial: X-ray diffraction of thin films, *J. Electroceram.*, 2021, **47**, 141–163, DOI: 10.1007/s10832-021-00263-6.

20 G. Gurieva, S. Niedenzu, N. Siminel, A. Franz and S. Schorr, The kesterite–stannite structural transition as a way to avoid Cu/Zn disorder in kesterites: the exemplary case of the $Cu_2(Zn, Mn)SnSe_4$, *Faraday Discuss.*, 2022, **239**, 51–69, DOI: 10.1039/D2FD00042C.

21 S. Schorr, H.-J. Hoebler and M. Tovar, A neutron diffraction study of the stannite-kesterite solid solution series, *Eur. J. Mineral.*, 2007, **19**(1), 65–73, DOI: 10.1127/0935-1221/2007/0019-0065.

22 M. Gansukh, Z. Li, M. E. Rodriguez, S. Engberg, F. M. A. Mortinho, S. L. Mariño, E. Stamate, J. Schou, O. Hansen and S. Canulescu, Energy band alignment at the heterointerface between CdS and Ag-alloyed CZTS, *Sci. Rep.*, 2020, **10**, 18388.

23 M. Dimitrievska, F. Boero, A. P. Litvinchuk, S. Delsante, G. Borzone, A. perez-Rodriguez and V. Izquierdo-Roca, Structural Polymorphism in "Kesterite" Cu_2ZnSnS_4: Raman Spectroscopy and First-Principles Calculations Analysis, *Inorg. Chem.*, 2017, **56**(6), 3467–3474, DOI: 10.1021/acs.inorgchem.6b03008.

24 S. Engberg, F. Martinho, M. Gansukh, A. Protti, R. Küngas, E. Stamate, O. Hansen, S. Canulescu and J. Schou, Spin-coated Cu_2ZnSnS_4 solar cells: a study on the transformation from ink to film, *Sci. Rep.*, 2020, **10**, 20749, DOI: 10.1038/s41598-020-77592-z.

25 S. Engberg, M. Gansukh, F. Martinho, E. Stamate, O. Hansen, J. Schou and S. Canulescu, Silver-substituted $(Ag_{1-x}Cu_x)2ZnSnS_4$ solar cells from aprotic molecular inks, *Ceram. Int.*, 2022, **48**(15), 21483–21491, DOI: 10.1016/j.ceramint.2022.04.116.

26 C. J. Bosson, M. T. Birch, D. P. Halliday, K. S. Knight, A. S. Gibbs and P. D. Hatton, Cation disorder and phase transitions in the structurally complex solar cell material Cu_2ZnSnS_4, *J. Mater. Chem. A*, 2017, **5**, 16672–16680, DOI: 10.1039/C7TA03603E.

27 M. Y. Valakh, O. F. Kolomys, S. S. Ponomaryov, V. O. Yukhymchuk, I. S. Babichuk, V. Izquierdo-Roca, E. Saucedo, A. Perez-Rodriguez, J. R. Morante, S. Schorr and I. V. Bodnar, Raman scattering and disorder effect in Cu_2ZnSnS_4, *Phys. Status Solidi RRL*, 2013, **7**(4), 258–261, DOI: 10.1002/pssr.201307073.

28 M. Dimitrievska, H. Xie, A. J. Jackson, X. Fontané, M. Espíndola-Rodríguez, E. Saucedo, A. Pérez-Rodríguez, A. Walsh and V. Izquierdo-Roca, Resonant Raman scattering of ZnS_xSe_{1-x} solid solutions: the role of S and Se electronic states, *Phys. Chem. Chem. Phys.*, 2016, **18**, 7632–7640, DOI: **10.1039/C5CP04498G**.

29 P. A. Fernandes, P. M. P. Salomé and A. F. da Cunha, Study of polycrystalline Cu2ZnSnS4 films by Raman scattering, *J. Alloys Compd.*, 2011, **509**(28), 7600–7606, DOI: **10.1016/j.jallcom.2011.04.097**.

30 L. S. Price, I. P. Parkin, A. M. E. Hardy, R. J. H. Clark, T. G. Hibbert and K. C. Molloy, Atmospheric Pressure Chemical Vapor Deposition of Tin Sulfides (SnS, Sn_2S_3, and SnS_2) on Glass, *Chem. Mater.*, 1999, **11**(7), 1792–1799, DOI: **10.1021/cm990005z**.

31 S. W. Shin, S. M. Pawar, C. Y. Park, J. H. Yun, J. Moon, J. H. Kim and J. Y. Lee, Studies on Cu_2ZnSnS_4 (CZTS) absorber layer using different stacking orders in precursor thin films, *Sol. Energy Mater.*, 2011, **95**(12), 3202–3206, DOI: **10.1016/j.solmat.2011.07.005**.

32 H. H. Nazari and T. P. Dhakal, Influence of Ag-doping on the performance of Cu_2ZnSnS_4 solar cells, *Sol. Energy*, 2023, **253**, 321–331, DOI: **10.1016/j.solener.2023.02.001**.

33 W. Li, X. Liu, H. Cui, S. Huang and X. Hao, The role of Ag in $(Ag, Cu)_2ZnSnS_4$ thin film for solar cell application, *J. Alloys Compd.*, 2015, **625**, 277–283, DOI: **10.1016/j.jallcom.2014.11.136**.

34 M. Danilson, M. Altosaar, M. Kauk, A. Katerski, J. Krustok and J. Raudoja, XPS study of CZTSSe monograin powders, *Thin Solid Films*, 2011, **519**(21), 7407–7411, DOI: **10.1016/j.tsf.2010.12.165**.

35 Y. Wu, Y. Zhang, Y. Sui, Z. Wang, S. Lv, M. Wei, Y. Sun, B. Yao, X. Liu and L. Yang, Bandgap engineering of $Cu_2In_xZn_{1-x}Sn(S, Se)_4$ alloy films for photovoltaic applications, *Ceram. Int.*, 2018, **44**(2), 1942–1950, DOI: **10.1016/j.ceramint.2017.10.137**.

36 S. Landi, I. R. Segundo, E. Freitas, M. Vasilevskiy, J. Carneiro and C. J. Tavares, Use and misuse of the Kubelka-Munk function to obtain the band gap energy from diffuse reflectance measurements, *Solid State Commun.*, 2022, **341**, 114573, DOI: **10.1016/j.ssc.2021.114573**.

37 P. Kubelka, New Contributions to the Optics of Intensely Light-Scattering Materials. Part I, *J. Opt. Soc. Am.*, 1948, **38**(5), 448–457, DOI: **10.1364/JOSA.38.000448**.

